Research Article Vol. 35, No. 2 / February 2018 / Journal of the Optical Society of America B 481

Journal of the Optical Society of America B

OPTICAL PHYSICS

High-speed time-domain balanced homodyne detector for nanosecond optical field applications

Shanna Du,[1] Zongyang Li,[1] Wenyuan Liu,[1] Xuyang Wang,[1,2] and Yongmin Li[1,2,*]

[1]State Key Laboratory of Quantum Optics and Quantum Optics Devices, Institute of Opto-Electronics, Shanxi University, Taiyuan 030006, China
[2]Collaborative Innovation Center of Extreme Optics, Shanxi University, Taiyuan 030006, China
*Corresponding author: yongmin@sxu.edu.cn

Received 6 November 2017; revised 5 January 2018; accepted 8 January 2018; posted 9 January 2018 (Doc. ID 312859); published 1 February 2018

We present a high-speed time-domain shot-noise-limited balanced homodyne detector that is suitable for the detection of the quantum states of nanosecond pulsed optical fields. The detector can detect the quantum noise of individual nanosecond optical pulses at a repetition rate of 40 MHz and achieve a signal-to-noise ratio of above 14.5 dB at a local oscillator power of 9.9×10^7 photons per pulse. The stability of the detector is characterized via an Allan variance measurement, and superior stability is observed. The detector is especially applicable in the fields of quantum optics and quantum information, where high-speed time-domain detection of nanosecond pulsed optical field quadratures is required.

OCIS codes: (270.5570) Quantum detectors; (060.2920) Homodyning; (270.5565) Quantum communications.

https://doi.org/10.1364/JOSAB.35.000481

1. INTRODUCTION

In quantum optics and quantum information processing, effective and reliable detection of optical quantum states is of great importance. Balanced homodyne detectors (BHDs), which use a pair of near-identical quantum efficiency photodiodes, provide a well-established technique for measuring the quadratures of an optical field by interfering the target signal field with a phase-referenced field (local oscillator, LO) at particular relative phases [1,2]. The homodyne detection technique enables complete characterization of the quantum state and quantum optical process, i.e., quantum-state tomography [3] and quantum process tomography [4]. Along with the single-photon detection technique, they constitute powerful tools for quantum optical metrology [5,6]. BHDs were initially designed for measurement of the quadratures of optical states in the frequency domain [7–12], where a specific frequency range (sideband) of the photocurrent difference signal is chosen to characterize the quantum noise of the optical states. Later, time-domain BHDs [13–21] were proposed, which could detect individual pulsed optical states in real time and output an electrical signal proportional to the single value of the pulsed optical field quadrature. For a signal field and LO in the same single spatial mode, the output electrical signal of the BHDs is

$$\hat{i}(\theta) \propto \hat{X}_S(\theta) = \int_0^{\tau_0} |\alpha_L(t)| \hat{X}_S(t,\theta) \mathrm{d}t, \tag{1}$$

where $\hat{X}_S(t,\theta) = (1/2)(\hat{a}_S(t)e^{-i\theta} + \hat{a}_S^{\dagger}(t)e^{i\theta})$ is the instantaneous quadrature of the pulsed signal field, τ_0 is the pulse duration, θ is the relative phase between the signal field and the LO, $\hat{X}_S(\theta)$ is the quadrature of the pulsed signal field projected onto the temporal mode of the LO, $\hat{a}_S(t)$ is the signal-field annihilation operators, and $|\alpha_L(t)|$ is the amplitude of the coherent LO, which is much stronger than that of the signal field.

With the rapid development of quantum information processing [22,23], pulsed time-domain BHDs have attracted increasingly more attention. For instance, in a continuous variable quantum key distribution system [24–27], a time-domain BHD is an essential measurement apparatus for detecting the quantum states of the pulsed optical fields where the key information is encoded. The secure key rate of the system is primarily determined by the bandwidth of the detectors. For high-speed time-domain BHDs, a broad spectral response region—from DC to higher than the repetition rate of the pulsed signal—is required to ensure clear discrimination of individual pulsed quantum states and guarantee sufficient signal amplification.

For a transimpedance or voltage preamplifier-based BHD, the area under each output electric pulse is proportional to the pulsed field quadrature if the pulse duration of the incident light is much longer than the response time of the photodiodes. This kind of detector could probe pulsed quantum states with a repetition rate above 100 MHz [17,21]. The limitation is that high-speed data acquisition and post-processing with a bandwidth much higher than the inverse of the pulse duration are necessary. If the pulse duration of the input light is

much shorter than the response time of the photodiodes, the photodiode's junction capacitance will integrate the photon current signal and the peak value of the detector output electric pulse will be proportional to the quadrature value of the signal field. This type of detector is suitable for detection of ultrafast pulsed quantum states with picosecond or femtosecond pulse durations [20]. However, for various applications, such as continuous variable quantum key distribution, the pulse width of the incident light is usually of the order of nanoseconds. In this case, the charge amplifier-based time-domain BHD is an effective approach [13,19]. In such scenarios, the charge amplifier effectively integrates the input photon current pulses and converts them into voltage pulses. The generated voltage signals are then AC-coupled to a pulse shaper through a pole zero differentiator. The bandwidth of detectors with such configurations is currently limited to the order of 1–2 MHz.

In this paper, we present a high-speed fiber-based time-domain BHD based on a charge-sensitive preamplifier. More precisely, we use a low input-noise operational amplifier with appropriate feedback capacitance and resistance to act as a low-noise charge amplifier. Instead of the pole zero differentiator and shaper amplifiers utilized in previous works, we designed an RLC high-pass filter (HPF) that effectively improves the bandwidth as well as the signal-to-noise ratio (SNR) of the BHD. Furthermore, a voltage amplifier followed by a low-pass filter (LPF) is utilized as the pulse shaper and amplifier. We show that the detector could probe nanosecond optical pulses with a repetition rate up to 40 MHz and an SNR above 14.5 dB at an LO power of 9.9×10^7 photons per pulse. The bandwidth of the proposed detector well surpasses the previous results with the charge amplifier configurations and can be further improved to accept a repetition rate of above 100 MHz for shorter input optical pulses.

2. DESIGN AND FABRICATION OF THE TIME-DOMAIN BHD DETECTOR

A schematic diagram of the time-domain BHD is shown in Fig. 1. Two photodiodes are wired in series and the generated pulse current difference is transmitted through capacitor C_1 (1 nF) and integrated by the feedback capacitance, C_f (0.7 pF), of the operational amplifier (ADA4817). The rise time and fall time of the output electrical pulse are determined by the pulse width of the input optical pulse and the time

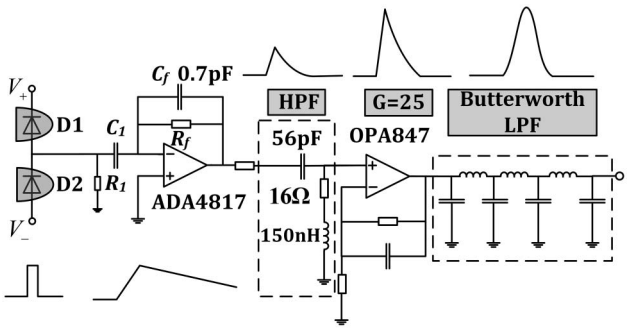

Fig. 1. Schematic of the BHD electronic circuit showing the main components. HPF, high-pass filter; LPF, seven-pole Butterworth low-pass filter.

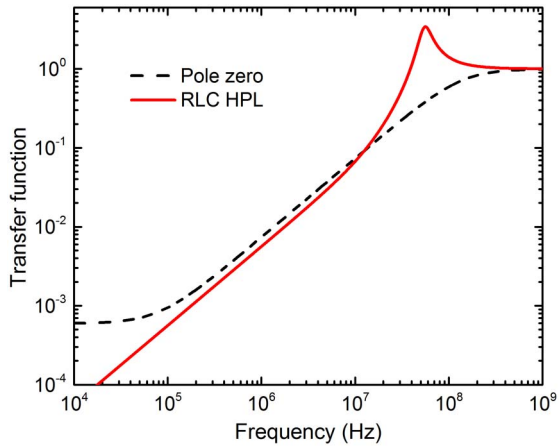

Fig. 2. Magnitude of the transfer functions for the pole zero differentiator and the RLC HPF.

constant $\tau = C_f \cdot R_f$, respectively. A subsequent RLC HPF is used to reduce the long falling time of the output electrical pulse. The filtered electrical signal is further amplified with a gain of $G = 25$ by an operational amplifier (OPA847) in a non-inverting configuration. Finally, the amplified electrical pulse is shaped by a seven-pole Butterworth LPF with a cutoff frequency of 140 MHz. Here, the LPF helps to smooth the peak of the electrical pulse and improve the SNR. To optimize the component values of the circuit for a target detector bandwidth and pulse shape, we analyzed the circuit with Multisim. The response characteristics predicted by the theoretical model closely matched the measured results of the detector.

As mentioned earlier, the bandwidth of the detector is fundamentally limited by the long falling time, τ, of the electrical pulse output from the charge preamplifier. Therefore, a careful design of the HPF is crucial to improving the bandwidth. Figure 2 depicts the theoretical simulation of the transfer function for two types of HPFs: the pole zero differentiator used in previous works [13,19] and the RLC HPF employed in the current detector. The transfer function of the RLC HPF is given by $H(f) = (R_H + i2\pi f L_H)/[R_H + i2\pi f L_H + 1/(i2\pi f C_H)]$, where f represents the frequency, and R_H, L_H, and C_H represent the resistance, capacitance, and inductance of the HPF. It is clear that the signal attenuation of the RLC HPF is higher than that of the pole zero differentiator when the signal frequency is less than 6 MHz. In the high-frequency range, in contrast to the pole zero differentiator, the RLC HPF exhibits better transfer characteristics, i.e., it presents lower attenuation levels. Due to the fact that RLC circuits are resonant circuits, a resonance peak around 56 MHz appeared in the response curve. The electronic dark noise of the charge preamplifier mainly produces low-frequency noise, whereas the signal pulse resides in the high-frequency range. Therefore, the RLC HPF could significantly improve the pulse repetition rate and suppress the electronic dark noise in comparison to the pole zero differentiator. By utilizing this kind of filter, we can improve the bandwidth of the time-domain BHD to the order of 100 MHz.

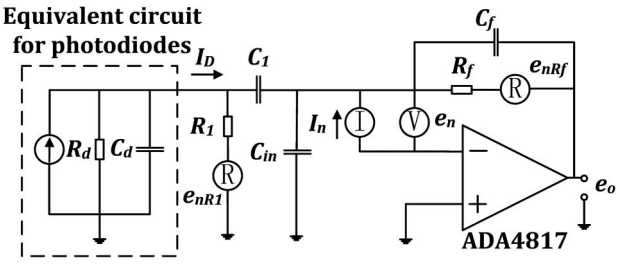

Fig. 3. Equivalent circuit diagram of the photodiodes and the charge preamplifier for noise analysis.

The SNR of the charge preamplifier plays a key role on the SNR of the detector. Therefore, we first analyze the sources of noise that originate from the voltage noise generated by the dark current noise of the photodiodes and the input current noise of the ADA4817, e_{noi}, the resistor thermal noise, e_{noR}, and the voltage noise from the input voltage noise of the ADA4817, e_{noe}. Figure 3 shows the equivalent circuit diagram of the photodiodes (dashed frame) and the charge preamplifier. In this figure, the shunt resistance and the junction capacitance of the photodiodes in parallel are denoted by R_d and C_d, respectively. The shot-noise current from the photodiodes' dark current, I_d, is denoted by I_D. The input current noise, input voltage noise, and differential-mode capacitance of the ADA4817 are I_n, e_n, and C_{in}, respectively. The shot-noise current, I_D, and input noise current, I_n, pass through the feedback resistor, R_f, and capacitor, C_f, and generate the noise voltage, e_{noi}, which is given by

$$e_{\mathrm{noi}} = (I_D + I_n)\cdot\frac{R_f}{1 + i\cdot 2\pi f R_f C_f} = \left(\sqrt{2e\cdot I_d} + I_n\right)\cdot\frac{R_f}{1 + i\cdot 2\pi f R_f C_f}, \tag{2}$$

where e is the electronic charge. The second noise source comes from the resistor's thermal noise voltage, which is expressed as $\sqrt{4kTR}$, where k is the Boltzmann constant and T is the absolute temperature. The corresponding thermal noise current is $\sqrt{(4kT)/R}$, which decreases with R. Because the resistance of R_d is 100 GΩ, its thermal noise can be ignored. The main thermal noise voltage is caused by R_1 and the feedback resistor, R_f. Similarly, the output noise voltage, e_{noR}, due to the thermal noise currents from R_1 and R_f is given by

$$e_{\mathrm{noR}} = \left(\sqrt{\frac{4\ \mathrm{K}T}{R_1}} + \sqrt{\frac{4\ \mathrm{K}T}{R_f}}\right)\cdot\frac{R_f}{1 + i\cdot 2\pi f R_f C_f}. \tag{3}$$

As shown in Fig. 3, R_d and R_1 are connected in parallel to form the input resistor of the ADA4817, so its resistance is essentially dominated by R_1, which has a resistance of 1 MΩ. The ADA4817 itself has an intrinsic input resistor of the order of hundreds of GΩ, so we ignore it here. Capacitors C_d and C_1 are connected in series and then in parallel with C_{in} to form the input capacitance, C_i, of the ADA4817: $C_i = [(C_d\cdot C_1)/(C_d + C_1)] + C_{\mathrm{in}}$. The total input impedance of the ADA4817, Z_1, is the parallel impedance of R_1 and C_i. From this, the third noise source—the output voltage noise, e_{noe}, caused by the amplification of the input voltage noise, e_n, of the ADA4817—is given by

$$e_{\mathrm{noe}} = e_n\cdot\frac{Z_1 + Z_2}{Z_1} = e_n\left[\frac{1/R_1 + 1/R_f + i\cdot 2\pi f(C_f + C_i)}{1/R_f + i\cdot 2\pi f C_f}\right], \tag{4}$$

where $Z_2 = R_f/(1 + i\cdot 2\pi f R_f C_f)$ is the feedback impedance of the charge amplifier.

In the section above, we have investigated the three dominant noise sources of the detector; each exhibits a different noise spectrum. The total noise power in the time domain is obtained by adding the power spectral density for each kind of noise and integrating them over the entire frequency range:

$$E_{\mathrm{no}}^2 = \int_0^\infty |e_{\mathrm{noi}}|^2\mathrm{d}f + \int_0^\infty |e_{\mathrm{noR}}|^2\mathrm{d}f + \int_0^\infty |e_{\mathrm{noe}}|^2\mathrm{d}f. \tag{5}$$

In the following analysis, we derive the amplitude of the signal generated by the incident pulsed light field. When the optical pulses are incident on the photodiodes, a signal charge pulse, Q, with a pulse width τ_0 is generated and integrated by the feedback capacitance, C_f, to produce an output voltage pulse, $e_{\mathrm{out}}(t)$. For $\tau_0 \ll \tau$, the voltage pulse increases rapidly to an amplitude of $-(Q/C_f)$ during the time τ_0 and then slowly discharges with time constant $\tau = C_f\cdot R_f$. The approximate expression for the $e_{\mathrm{out}}(t)$ is given by

$$e_{\mathrm{out}}(t) = -\frac{Q}{C_f}\cdot e^{-t/\tau}. \tag{6}$$

As can be seen from the above equation, the signal charge pulse, Q, is converted into a voltage pulse with amplitude

$$E_{\mathrm{out}} = -\frac{Q}{C_f}. \tag{7}$$

Combining Eqs. (5) and (7), the SNR of the time-domain BHD is written as

$$\mathrm{SNR} = \frac{E_{\mathrm{out}}^2}{E_{\mathrm{no}}^2}. \tag{8}$$

From Eq. (7), it is evident that a smaller feedback capacitance, C_f, is beneficial to the signal amplitude, but it also increases the electrical noise according to Eqs. (2)–(4). Nevertheless, simulation shows that the increase in the signal amplitude is faster than that of the electrical noise. Thus, a small feedback capacitance improves the SNR of the detector.

Assuming a vacuum field input, we use the following experimental parameters to estimate the SNR: pulse width of $\tau_0 = 4$ ns, LO power of $\overline{n}_L = 6.1\times 10^7$ photons per pulse, and 80% quantum efficiency for the photodiodes. In this case, we have $Q = \sqrt{0.8\overline{n}_L}e$ and the theoretical SNR of the charge preamplifier is calculated to be 11.6 dB using Eq. (8). Considering further the effect of the RLC HPF, second stage amplifier, and the LPF, the final SNR of the detector can be determined to be ∼14 dB.

The performance of the circuit components strongly affects the SNR and bandwidth of the detector. First, we chose passive surface mount components that possess low noise, high

precision, and a superior high-frequency response. For the photodiodes, we chose fiber-pigtailed InGaAs PIN photodiodes with bandwidths of 6 GHz, quantum efficiencies of 80%, and 20 pA of dark current. The ADA4817 with field-effect transistor (FET) input was selected for the main part of the charge preamplifier because of its ultralow noise (4 nV/$\sqrt{\text{Hz}}$ and 2.5 fA/$\sqrt{\text{Hz}}$ at 100 kHz) as well as its very low input differential-mode capacitance (0.1 pF), so that the input noise is greatly reduced and a high SNR can be guaranteed. To amplify the pulsed voltage signal output from the charge preamplifier, the OPA847 voltage feedback operational amplifier—with a high gain bandwidth of 3.9 GHz and input voltage noise of 0.85 nV/$\sqrt{\text{Hz}}$—was selected as the second-stage voltage amplifier.

The layout of the printed circuit board is another non-negligible factor for the performance of the detector. The parasitic capacitance and inductance from the circuits may change the behavior of the circuits and introduce unexpected noises; such kind of parasitic phenomenon should be reduced as much as possible. The signal tracks for each photodiode before their joint point are well balanced to obtain a high commode mode rejection ratio. The power lines are kept away from the signal line to avoid potential interference to the AC signal. Finally, to avoid electromagnetic interference from the environment, the detector is enclosed in a shielding metal box which is connected to the circuit ground.

3. CHARACTERIZATION OF DETECTOR PERFORMANCE

Figure 4 shows the experimental setup used to test the performance of the detector. A fiber laser source delivers a 100 mW continuous-wave single-frequency laser at 1550 nm. The laser is attenuated by an adjustable fiber attenuator and injected into an amplitude modulator, which is driven by a pulse generator. After amplitude modulation, the generated optical pulses—with a 40 MHz repetition rate and a 4 ns pulse width—serve as the LO light. The signal mode interferes with the LO pulse at a 50:50 fiber splitter and then travels to the two photodiodes of the detector. For a shot-noise-limited time-domain BHD, the photocurrent signals generated from each photodiode should be well balanced in both intensity and arrival time. To this end, a variable optical attenuator—created by bending the pigtail fiber of the photodiode—was utilized. This method effectively compensates for the photodiode's quantum efficiency and the slight imbalance from the fiber beam splitter without extra insert loss. To balance the arrival times of the incident optical pulses, we first matched the path delay to be within 2 mm, then

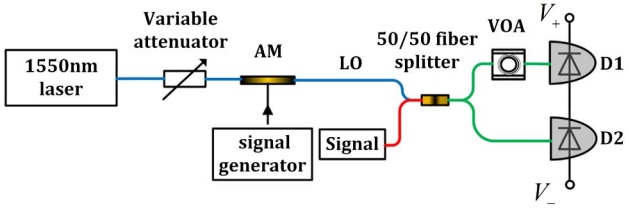

Fig. 4. Experimental setup for characterization of the time-domain BHD. AM, amplitude modulator; VOA, variable optical attenuator.

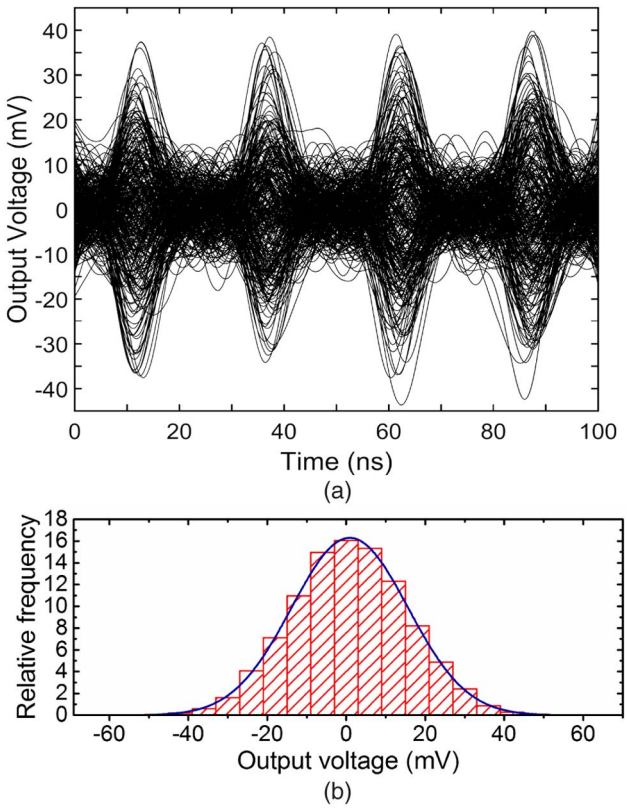

Fig. 5. (a) Time traces of the time-domain BHD output at a repetition rate of 40 MHz: LO power is 3.8×10^7 photons per pulse. (b) Histogram of the quadrature values for the vacuum field. Solid curve denotes the Gaussian fit.

a fine tuning is made by adjusting the bias voltage of the two photodiodes.

Figure 5(a) shows typical time traces of the BHD detector output voltage signal for a vacuum field input. We can see that the repetition rate of the detector is 40 MHz and the full width of the output electrical pulse is approximately 15 ns. The peak value of each electric pulse is proportional to the single quadrature value of the vacuum field, which is selected by the temporal and spatial mode of the LO pulse. The statistical distribution for the noise of the electrical pulse peaks originates from the quantum fluctuation of the vacuum field quadrature. Figure 5(b) plots a typical statistical histogram of the quadrature values for the vacuum field. The data were obtained from the peak values of a sequence of 10^6 pulses. It is clear that the measured results agree well with the Gaussian distribution, as expected for a vacuum state.

The bandwidth of the detector, i.e., the capability to distinguish individual optical pulses, affects the accuracy of the measured quadrature. To ensure each laser pulse is detected individually without correlation to other pulses, we investigated the correlation coefficient (CC) between subsequent vacuum quadrature values, which are inherently uncorrelated. To this end, we recorded the quadrature values of the vacuum field pulses at a repetition rate of 40 MHz and defined the CC as follows:

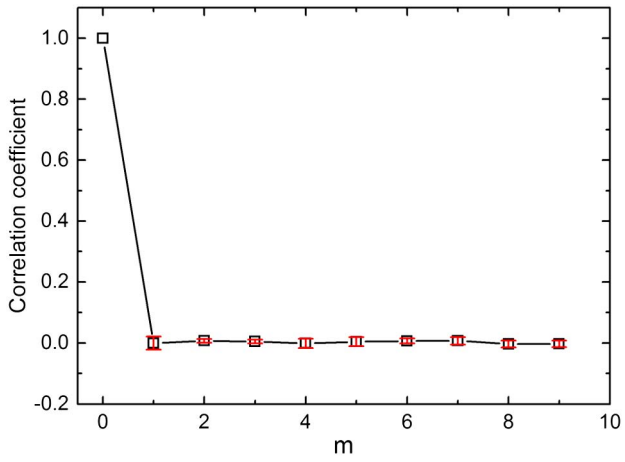

Fig. 6. Correlation coefficient between n-th and $(n+m)$-th pulses.

$$\mathrm{CC}(m) = \frac{\langle x_n x_{n+m}\rangle - \langle x_n\rangle\langle x_{n+m}\rangle}{\sqrt{\langle x_n^2\rangle - \langle x_n\rangle^2}\sqrt{\langle x_{n+m}^2\rangle - \langle x_{n+m}\rangle^2}}, \tag{9}$$

where the angle brackets indicate an average over the measured values ($n = 1, \ldots, 5000$), and x_n and x_{n+m} are the quadrature values of the vacuum field pulses separated by m periods. The calculated CC as a function of m for $m = 0, \ldots, 9$ is plotted in Fig. 6; we can see clearly that a complete correlation occurs when $m = 0$, whereas the correlation vanishes for $m \neq 0$. By evaluating the CC, we confirm that the detector achieves a bandwidth of at least 40 MHz, i.e., the detector can distinguish individual optical pulses at a repetition rate of 40 MHz.

By varying the input LO power from 1×10^6 to 9.9×10^7 photons per pulse with the variable optical attenuator, we measured the output peak values of the detector as a function of the LO power for a vacuum field input. For each LO power, 10^5 data points were recorded and the corresponding variance was calculated. In this way, the linearity and the SNR of the detector could be evaluated. As shown in Fig. 7, the shot noise variance, which was obtained by subtracting the electrical dark noise background from the variance of peak values, scales linearly with the LO power up to 9.9×10^7 photons per pulse.

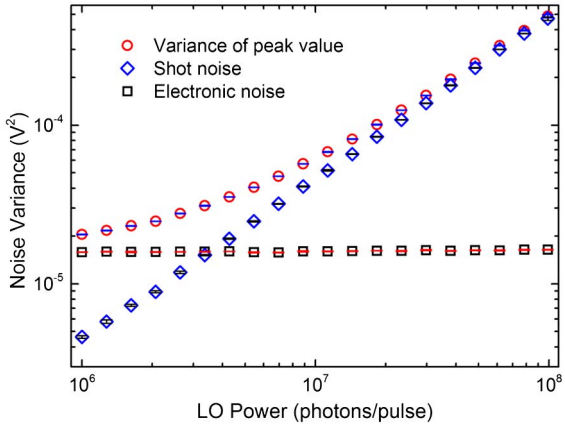

Fig. 7. Noise variance for the detector, measured in the time-domain as a function of the LO power for vacuum field input. The electronic dark noise is 1.6×10^{-5} V^2.

The observed linear dependence clearly confirms that the detector is shot-noise-limited over a wide range of LO powers. The corresponding SNR at an LO power of 9.9×10^7 photons per pulse is 14.5 dB. For an input LO power of 6.1×10^7 photons per pulse, the measured SNR is 12.6 dB, which is in good agreement with the theoretically predicted value (14 dB).

The stability of the detector is crucial for long-term accurate measurement of quantum states. Because each LO pulse typically contains 10^8 photons and the corresponding photon thus fluctuates on the order of 10^4, even a slight modification of the relevant parameters can result in significant imbalance for the detector. In practice, these relevant parameters include the variations of the 50:50 beam-splitter ratios and changes to the photodiode bias voltages. The imbalance of the detector inevitably leads to a shift of the detector baseline, which usually presents linear drift over a short time and slow oscillations over long periods of time. The drift of the detector baseline will cause detection errors in the measured quadrature values of an unknown quantum state. Although such imbalance can be calibrated at regular intervals, it is important to evaluate the stability of the detector to acquire the frequency of the calibration.

To perform a quantitative analysis of the baseline drift, we continuously collected the peak values of 10^5 detector output pulses at an acquisition rate of 1 kHz for 100 s. We then used the measured vacuum state quadratures to calculate the Allan variance, $\sigma^2(\tau)$ [14,16]:

$$\sigma^2(\tau) = \frac{1}{2}\langle(\overline{X}_{n+1} - \overline{X}_n)^2\rangle, \tag{10}$$

where $\overline{X}_{n+1}$ and $\overline{X}_n$ are averages of the measured quadratures of the vacuum state over adjacent intervals of length τ and the angle bracket indicates an average over all data. Equation (10) can be rewritten in detail as

$$\sigma^2(\tau) = \frac{1}{2}\cdot\frac{1}{N/m-1}\cdot\sum_{n=0}^{N/m-2}\left(\frac{1}{\tau}\sum_{i=n\cdot m}^{(n+1)\cdot m-1}(x_{i+m} - x_i)\right)^2, \tag{11}$$

where x_i is the measured quadrature value, $\tau_0 = 1$ ms is the time interval between adjacent x_i, N is the total number of data samples, and m is the number of sampling points over time

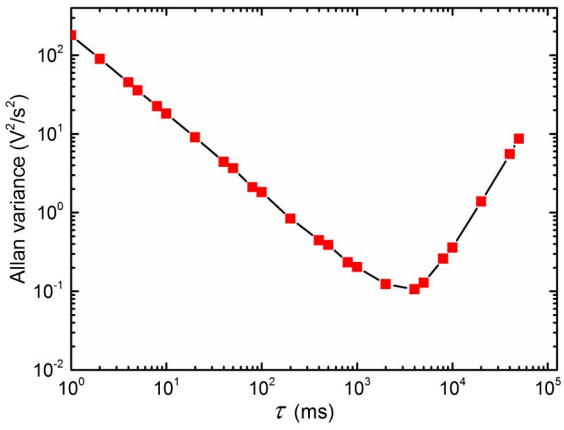

Fig. 8. Allan variance of the peak value of the detector output pulse for a period of 100 s.

$\tau \geq \tau_0$ with $\tau = m\tau_0$. Figure 8 shows the Allan variance calculated from the measured quadratures of the vacuum state in different time scales. For a total measurement time of 100 s, τ achieves its maximum value at 50 s, i.e., only two adjacent intervals exist in the dataset. We can see from Fig. 8 that the Allan variance, $\sigma^2(\tau)$, reaches its minimum at $\tau = 4$ s, which means that the detector drift is not significant in this time period. Therefore, the time-domain BHD can remain stable for at least 4 s without any calibration.

4. CONCLUSIONS

In summary, we designed and built a high-speed time-domain BHD that can individually measure nanosecond pulsed optical fields at repetition rates of 40 MHz. The detector exhibits an SNR above 14.5 dB at an LO power of 9.9×10^7 photons per pulse. Through the analysis of the CC from the recorded peak values of the vacuum field, we concluded that the detector achieved a bandwidth of at least 40 MHz. The noise of the detector output (after subtracting the electronic dark noise) was linearly dependent on the input LO power, which clearly confirmed the shot-noise-limited performance of the detector. Based on the calculated Allan variance, the detector could continuously measure pulsed quantum states for 4 s without calibration. We anticipate that the detector will be useful for various applications in the fields of quantum optics and quantum information processing. It should be noted that the detector could, in principle, be further improved to reach bandwidths beyond 100 MHz if a pulsed optical laser with a narrower pulse width (~1 ns) was utilized.

Funding. Key Project of the National Key R&D Program of China (2016YFA0301403); National Natural Science Foundation of China (NSFC) (61378010, 11774209, 11504219); Shanxi 1331KSC; Program for the Outstanding Innovative Teams of Higher Learning Institutions of Shanxi.

REFERENCES

1. H. P. Yuen and V. W. S. Chan, "Noise in homodyne and heterodyne detection," Opt. Lett. **8**, 177–179 (1983).
2. G. L. Abbas, V. W. S. Chan, and S. T. Yee, "Local-oscillator excess-noise suppression for homodyne and heterodyne detection," Opt. Lett. **8**, 419–421 (1983).
3. A. I. Lvovsky and M. G. Raymer, "Continuous-variable optical quantum-state tomography," Rev. Mod. Phys. **81**, 299–332 (2009).
4. M. Lobino, D. Korystov, C. Kupchak, E. Figueroa, B. C. Sanders, and A. I. Lvovsky, "Complete characterization of quantum-optical process," Science **322**, 563–566 (2008).
5. V. Giovannetti, S. Lloyd, and L. Maccone, "Advances in quantum metrology," Nat. Photonics **5**, 222–229 (2011).
6. J. H. Shapiro, "Parity measurements versus dual-homodyne measurements in coherent-state Mach-Zehnder interferometry," J. Opt. Soc. Am. B **34**, 1699–1704 (2017).
7. R. E. Slusher, L. W. Hollberg, B. Yurke, J. C. Mertz, and J. F. Valley, "Observation of squeezed states generated by four-wave mixing in an optical cavity," Phys. Rev. Lett. **55**, 2409–2412 (1985).
8. O. Morin, K. Huang, J. L. Liu, H. Le Jeannic, C. Fabre, and J. Laurat, "Remote creation of hybrid entanglement between particle-like and wave-like optical qubits," Nat. Photonics **8**, 570–574 (2014).
9. L. Wu, Y. H. Liu, R. J. Deng, Z. H. Yan, X. J. Jia, and K. Peng, "Deterministic generation of bright polarization squeezed state of light resonant with the rubidium D1 absorption line," J. Opt. Soc. Am. B **33**, 2296–2301 (2016).
10. T. Serikawa, J. I. Yoshikawa, K. Marino, and A. Frusawa, "Creation and measurement of broadband squeezed vacuum from a ring optical parametric oscillator," Opt. Express **24**, 28383–28391 (2016).
11. J. Y. Haw, J. Zhao, J. Dias, S. M. Assad, M. Bradshaw, R. Blandino, T. Symul, T. C. Ralph, and P. K. Lam, "Surpassing the no-cloning limit with a heralded hybrid linear amplifier for coherent states," Nat. Commun. **7**, 13222 (2016).
12. N. Wang and Y. M. Li, "Quantum analysis and experimental investigation of the nondegenerate optical parametric oscillator with unequally injected signal and idler," Phys. Rev. A **93**, 013831 (2016).
13. H. Hansen, T. Aichele, C. Hettich, P. Lodahl, A. I. Lvovsky, J. Mlynek, and S. Schiller, "Ultrasensitive pulsed, balanced homodyne detector: application to time-domain quantum measurements," Opt. Lett. **26**, 1714–1716 (2001).
14. A. Zavatta, M. Bellini, P. L. Ramazza, F. Marin, and F. T. Arecchi, "Time-domain analysis of quantum states of light: noise characterization and homodyne tomography," J. Opt. Soc. Am. B **19**, 1189–1194 (2002).
15. R. Okubo, M. Hirano, Y. Zhang, and T. Hirano, "Pulse-resolved measurement of quadrature phase amplitudes of squeezed pulse trains at a repetition rate of 76 MHz," Opt. Lett. **33**, 1458–1460 (2008).
16. O. Haderka, V. Michalek, V. Urbasek, and M. Jezek, "Fast time-domain balanced homodyne detection of light," Appl. Opt. **48**, 2884–2889 (2009).
17. Y. M. Chi, B. Qi, W. Zhu, L. Qian, H. K. Lo, S. H. Youn, A. I. Lvovsky, and L. Tian, "A balanced homodyne detector for high-rate Gaussian-modulated coherent-state quantum key distribution," New J. Phys. **13**, 013003 (2011).
18. R. Kumar, E. Barrios, A. MacRae, E. Cairns, E. H. Huntington, and A. I. Lvovsky, "Versatile wideband balanced detector for quantum optical homodyne tomography," Opt. Commun. **285**, 5259–5267 (2012).
19. X. Y. Wang, Z. L. Bai, P. Y. Du, Y. M. Li, and K. C. Peng, "Ultrastable fiber-based time-domain balanced homodyne detector for quantum communication," Chin. Phys. Lett. **29**, 124202 (2012).
20. M. Cooper, C. Söller, and B. J. Smith, "High-stability time-domain balanced homodyne detector for ultrafast optical pulse applications," J. Mod. Opt. **60**, 611–616 (2013).
21. D. Huang, J. Fang, C. Wang, P. Huang, and G. H. Zeng, "A 300-MHz bandwidth balanced homodyne detector for continuous variable quantum key distribution," Chin. Phys. Lett. **30**, 114209 (2013).
22. U. L. Andersen, G. Leuchs, and C. Silberhorn, "Continuous-variable quantum information processing," Laser Photon. Rev. **4**, 337–354 (2009).
23. C. Weedbrook, S. Pirandola, R. García-Patrón, N. J. Cerf, T. C. Ralph, J. H. Shapiro, and S. Lioyd, "Gaussian quantum information," Rev. Mod. Phys. **84**, 621–669 (2012).
24. F. Grosshans, G. Van Assche, J. Wenger, R. Brouri, N. J. Cerf, and P. Grangier, "Quantum key distribution using Gaussian-modulated coherent states," Nature **421**, 238–241 (2003).
25. E. Diamanti and A. Leverrier, "Distributing secret keys with quantum continuous variables: principle, security and implementations," Entropy **17**, 6072–6092 (2015).
26. Y. M. Li, X. Y. Wang, Z. L. Bai, W. Y. Liu, S. S. Yang, and K. C. Peng, "Continuous variable quantum key distribution," Chin. Phys. B **26**, 040303 (2017).
27. E. Diamanti, H. K. Lo, B. Qi, and Z. L. Yuan, "Practical challenges in quantum key distribution," npj Quantum Inform. **2**, 16025 (2016).